Surfaces and Interfaces 73 (2025) 107611

Contents lists available at ScienceDirect

Surfaces and Interfaces

journal homepage: www.sciencedirect.com/journal/surfaces-and-interfaces

Piezo-Triggered Formation of Functional ZnO@Au Interfaces: Toward Instant and Sustainable Interface Engineering

Simona Bettini [a,b,*], Gabriele Manca [a,c], Rosanna Pagano [a], Chiara Ingrosso [d], Donato Valli [e], Johan Hofkens [e], Maarten Roeffaers [f], Ludovico Valli [a,b], Gabriele Giancane [b,g]

[a] Dipartimento di Scienze e Tecnologie Biologiche e Ambientali, Università del Salento, Via Monteroni, Lecce, I-73100, Italy
[b] Consorzio Interuniversitario Nazionale per la Scienza e la Tecnologia dei Materiali, INSTM, Via G. Giusti, Firenze, I-50121, Italy
[c] Department of Chemistry, Biology and Biotechnology, Centro di Eccellenza per i Materiali Innovativi Nanostrutturati (CEMIN), University of Perugia, via Elce di Sotto 8, Perugia, 06123, Italy
[d] CNR-IPCF Bari Division, Via Orabona 4, Bari, 70125, Italy
[e] Department of Chemistry, KU Leuven, Celestijnenlaan 200F, Heverlee 3001, Belgium
[f] Centre for Membrane Separations, Department of Microbial and Molecular Systems, Adsorption, Catalysis and Spectroscopy for Sustainable Solutions, KU Leuven, Celestijnenlaan 200F, 3001 Leuven, Belgium
[g] Department of Cultural Heritage, University of Salento, Via D. Birago 64, Lecce, 73100, Italy

ARTICLE INFO

KEYWORDS:
Zinc Oxide
Gold Nanoparticles
Piezoelectric Effect
H_2O_2 Photocatalysis
Cr(VI) photoreduction
Oxygen Reduction Reaction

ABSTRACT

We report an ultra-rapid and sustainable method for the fabrication of metal–semiconductor hybrid interfaces via piezoelectrically-assisted ultrasound activation. A one-minute sonication of zinc oxide (ZnO) nanoflowers in aqueous Au^{3+} solution induces the *in situ* nucleation of gold nanoparticles (AuNPs), driven by local piezopotentials generated through cavitation. This reagent-free and low-energy process yields tunable surface architectures with AuNPs selectively decorating the ZnO interface, in the absence of external reducing agents, surfactants, light, or heat. Structural and spectroscopic analyses (TEM, XRD, Raman) reveal a controlled modification of both surface and sub-surface regions, confirming interface-level coupling between the semiconductor and the metal phase. The photocatalytic performance of the resulting ZnO@Au hybrids was explored as a proof of interfacial functionality, using two representative redox reactions: selective H_2O_2 generation via a two-step oxygen reduction pathway, and Cr(VI) photoreduction in aqueous solution. In both cases, catalytic activity was strongly dependent on nanoparticle size and interfacial distribution. Scavenger experiments further supported the proposed mechanisms, highlighting the role of AuNPs in facilitating charge separation and enhancing photocatalytic selectivity. The results offer new insights for the design of functional nanointerfaces for catalysis, environmental remediation, and light-driven surface processes.

1. Introduction

Hybrid metal–semiconductor nanostructures are at the forefront of interface engineering due to their unique ability to couple electronic, optical, and catalytic properties across distinct material domains [1,2]. By integrating plasmonic metals, such as gold, with wide-bandgap semiconductors like zinc oxide (ZnO), it becomes possible to create multifunctional interfaces capable of driving charge transfer processes with enhanced functionalities [3–7]. This synergy at the nanoscale [8,9] opens avenues for applications in photocatalysis, sensing, pollutant remediation, and energy conversion [10–13].

A central challenge in this field is the development of controlled, scalable, and environmentally benign methods to fabricate such hybrid interfaces [14]. Traditional physical and chemical approaches—such as sputtering, photoreduction, or colloidal deposition—often require high temperatures, chemical reducing agents, or lengthy multi-step procedures that can limit reproducibility and sustainability [15–17]. In this context, ultrasound-assisted synthesis appears as a promising route, particularly when leveraging the intrinsic piezoelectric properties of materials like ZnO. Mechanical stress induced by cavitation phenomena during sonication can generate internal piezopotentials, which, in turn, facilitate redox processes at the material surface without external irradiation or added chemicals [18,19].

Here, we present a novel and ultra-rapid method for the synthesis of

* Corresponding author.
E-mail address: simona.bettini@unisalento.it (S. Bettini).

https://doi.org/10.1016/j.surfin.2025.107611
Received 16 June 2025; Received in revised form 25 August 2025; Accepted 4 September 2025
Available online 4 September 2025

ZnO@Au hybrid nanostructures through piezoelectrically-assisted sonochemistry. In our approach, ZnO nanoflowers are simply dispersed in aqueous Au^{3+} solution and exposed to ultrasonic stimulation (42 kHz) for just one minute. This brief mechanical activation is sufficient to trigger the in situ reduction of gold ions and the direct nucleation of Au nanoparticles (AuNPs) at the ZnO surface. Unlike conventional methods, this process does not require light, heat, organic solvents, or external reducing agents [20–22], making it highly attractive for green nanofabrication. The resulting ZnO@Au materials exhibit tuneable AuNP size and density, controlled by simply modifying the gold precursor concentration.

Structural and spectroscopic analyses (TEM, XRD, Raman) reveal that the gold nanoparticles are not only deposited on the surface but also induce detectable modifications in the ZnO lattice, indicating a level of interfacial integration relevant for charge separation and surface chemistry. To validate the interfacial reactivity of the resulting ZnO@Au hybrids, we explored two benchmark redox processes: the two-electron oxygen reduction to hydrogen peroxide (H_2O_2), and the photoreduction of Cr(VI) to Cr(III), both relevant to environmental remediation and energy applications [23–25]. The dual functionality demonstrated in these applications highlights the broad catalytic spectrum of the synthesized nanointerfaces and underscores the generalizability of the approach. In this context, the present work primarily aims to emphasize the ease and versatility of the synthesis method for ZnO-based hybrid nanostructures, with the reported photocatalytic tests serving as proof-of-concept demonstrations of their photoactivity.

This study advances a new paradigm in photocatalyst fabrication which is ultra-rapid, green, and scalable allowing access to interfacial architectures that are inherently functional for promising avenues in photocatalytic design, environmental nanotechnology, and interfacial materials science.

2. Experimental Section

2.1. Synthesis of ZnO@Au hybrids

Flower-like shaped ZnO microstructures were synthetized according to a previously reported procedure [26].

ZnO@Au hybrid materials (A1, B1, C1, D1) were prepared by mixing 2 mg of ZnO with different volumes of $HAuCl_4 3H_2O$ (≥ 99%, Merck), starting from a 5×10^{-3} M stock solution dissolved in ethanol (96%, Merck) as detailed in Table 1, in 2 mL final volume of Milli-Q water-ethanol mixture in a 1.5:1 v:v ratio. The resulting solutions were then subjected to ultrasonic treatment for 1 min in a conventional laboratory ultrasonic bath (42 kHz, 100 W) at room temperature and in the dark. Subsequently, the suspensions were allowed to undergo gravimetric precipitation in the dark for approximately 20 min, after which the supernatant was removed. The precipitates were washed three times with Milli-Q water and air-dried overnight in the dark. Finally, the powders were collected and stored in the dark for further characterization and investigation.

Colloidal suspensions of ZnO in the presence of a $HAuCl_4$ solution were prepared according to line D1 of Table 1 and treated under static illumination, upon static contact and under vigorous stirring for 10 min.

Table 1
ZnO powder/Au precursor mixtures' composition for ultrasounds assisted synthesis of the ZnO@Au hybrids.

	ZnO	$[HAuCl_4 3H_2O]$ 5×10^{-3}M	Ethanol	H_2O
A1	2 mg	-	800 μL	1.2 mL
B1	2 mg	8 μL	792 μL	1.2 mL
C1	2 mg	40 μL	760 μL	1.2 mL
D1	2 mg	200 μL	600 μL	1.2 mL

2.2. Morphological and physical-chemical characterization

Raman spectroscopy was conducted on the synthesized materials in powder form, using a 532 nm laser at a power density of 0.125 mW/cm^2. Each spectrum was acquired in the 100–1000 cm^{-1} range using a Horiba Xplora microRaman.

Powder X-ray diffraction (PXRD) patterns were recorded with a Malvern PANalytical Empyrean diffractometer operating in transmission mode. The instrument was equipped with a PIXcel3D solid-state detector and a Cu anode. The diffractogram was recorded in the range of 2θ between 5 and 45° with a step size of 0.131°.

Analysis through Transmission Electron Microscopy (TEM) was conducted using a Jeol Jem-1011 microscope, operating at 100 kV. The microscope featured a high-contrast objective lens and a tungsten filament as the electron source, offering a point resolution of 0.34 nm. Image acquisition was performed with an 11-megapixel Quemesa Olympus CCD camera. Sample preparation involved immersing a 300-mesh copper grid coated with amorphous carbon into an ethanol-based dispersion of the samples, followed by solvent evaporation. The sizes of the gold nanostructures on ZnO were estimated using ImageJ software by analyzing images of each hybrid nanostructure deposited on multiple TEM grids.

Field Emission Scanning Electron Microscopy (FE-SEM) analysis was carried out using a Zeiss Sigma microscope, operated within the 0–10 kV range and equipped with an in-lens secondary electron detector as well as an INCA Energy Dispersive Spectroscopy (EDS) system. The specimens were fixed onto stainless-steel stubs using double-sided conductive carbon tape and electrically grounded with silver paste.

Samples were dissolved at 0.6 g L^{-1} final concentration in Milli-Q water for fluorescence emission spectroscopy analyses, carried out by using a Horiba Jobin Yvon Fluorolog spectrophotometer at an excitation wavelength of 370 nm. The same dispersion where further investigated by UV-Vis absorption spectroscopy to determine the absorbance intensity at 370 nm by a Cary 5000 (Agilent) spectrophotometer.

2.3. Photocatalytic experiments

2.3.1. Photocatalytic H_2O_2 production and quantification

Hydrogen peroxide (H_2O_2) production was evaluated following the POD-KI test [27]. In this method, H_2O_2 oxidizes iodide (I^-) to iodine (I_2) in the presence of the peroxidase enzyme (POD) (≥250 units/mg, Merck) (eq. 1). The liberated iodine subsequently reacts to form triiodide (I_3^-), a yellow-colored complex (eq. 2), the intensity of which, spectrophotometrically measured at 350 nm, is directly proportional to the concentration of H_2O_2.

$$H_2O_2 + 2I^- + 2H^+ \rightarrow 2H_2O \quad (1)$$

$$I_2 + I^- \rightarrow I_3^- \quad (2)$$

To obtain a calibration curve, a solution containing 1 mL of 1 M KI (Merck) stock solution, 0.25 mL of 100 units mL^{-1} POD stock solution (dissolved in 0.5 M phosphate saline buffer, PBS, at pH 6), 2.5 mL of 0.5 M PBS at pH 6, 20.75 mL of Milli-Q water, was prepared. Then, 0.5 mL of standard solutions at different concentrations of H_2O_2 (30%, Merck) were mixed with 0.5 mL of the above-described solution (POD-KI solution) and left interacting for 15 sec, before recording the UV-Vis absorption spectra with a Cary 5000 instrument. The absorbance value at 350 nm was monitored.

For the quantification of the produced H_2O_2, 0.6 g L^{-1} aqueous mixtures of the samples (A1, B1, C1 and D1) were prepared in Milli-Q water and kept under very gentle stirring for the entire duration of the experiment. The dispersion was then irradiated for 30 minutes using a LOT-Oriel Solar S class A (0.1 W cm^{-2} light intensity) solar simulator (https://www.nrel.gov/grid/solar-resource/spectra.html), positioned approximately 10 cm from the sample. At the end of the irradiation period, the solution was centrifuged, and 0.5 mL of the supernatant was

mixed with 0.5 mL of POD-KI solution, allowing the reaction to proceed for 15 sec.

Further, the Apparent Quantum Yield (AQY %) [28] for H_2O_2 production was calculated using the equation reported below:

$$AQY\ (\%) = \frac{2\ \times n(H_2O_2)}{N_{photons}}\ x\ 100 \quad (3)$$

Where $n(H_2O_2)$ refer to the number of the molecules and $N_{photons}$ is the number of absorbed photons, whis was determined based on the incident light power and the catalyst's absorbance at 370 nm (eq. 4 and eq. 5).

$$N_{photons} = \frac{P \times t \times \lambda}{h\ \times c}\ x\ A \quad (4)$$

$$A = 1 - 10^{-Abs} \quad (5)$$

Where P is the incident light power (W), t is the time (sec), λ is the wavelength corresponding to ZnO maximum absorption band (m), h is the Plank constant and c the light speed.

This metric is essential for evaluating the efficiency of the photocatalyst in converting light energy into chemical energy and so fundamental to compare the performance of the developed hybrid systems.

2.3.2. Scavenging tests for H_2O_2 production

H_2O_2 production mechanism was investigated for A1, B1, C1 and D1 samples by means of reactive species scavenging tests; specifically, 2-propanol (ACS reagent, ≥99.5 %, Merck) and ascorbic acid (Merck) were used to scavenge hydroxyl radicals and superoxide ions, respectively. The H_2O_2 photoproduction experiments with 1 mM of these scavengers were carried out as reported in the previous paragraph.

2.3.3. Reusability experiments for H_2O_2 production

The recyclability of D1 photocatalyst was evaluated over four consecutive reaction cycles. After each cycle, the catalyst was recovered by centrifugation and washed thoroughly with Milli-Q water. The reaction conditions were maintained constant across all cycles to assess the catalyst's stability and performance. The photocatalytic activity was monitored by measuring the production of H_2O_2 in each cycle. The catalyst's performance over four cycles was evaluated by calculating the relative H_2O_2 production, expressed as the molar concentration of H_2O_2 at each cycle relative to that in the first cycle (%): $\frac{[H_2O_2]n}{[H_2O_2]1st\ cycle}\ x100$. This allowed for assessing any potential deactivation or loss of catalytic activity over repeated use.

2.3.4. Cr(VI) Photoreduction experiments

The Cr(VI) – Cr(III) photoreduction experiments were carried out using ZnO-based catalysts (A1, B1, C1, D1) at a concentration of 0.6 g L^{-1}. A 3 × 10^{-3} M aqueous (ultrapure water) solution of potassium dichromate ($K_2Cr_2O_7$, Merck) was prepared and adjusted to pH 4 using 0.1 M sulfuric acid (H_2SO_4, Merck). The total reaction volume was 2 mL. The suspension was irradiated using a LOT-Oriel Solar S class A (0.1 W cm^{-2} light intensity) solar simulator, positioned approximately 10 cm from the sample; the reaction was kept under gentle stirring. At each time point (every 10 min), the solution was centrifuged and the supernatant was characterized by UV-Vis spectroscopy.

Absorbance changes at 450 nm and 620 nm were monitored to track the reduction of $Cr_2O_7^{2-}$. Control experiments were also conducted: one under illumination without the catalyst, and another in the dark with D1 catalyst.

2.3.5. Scavenging tests for dichromate reduction

Dichromate photoreduction mechanism was investigated for A1, B1, C1 and D1 samples by means of reactive species scavenging tests; specifically, p-benzoquinone, Q_0, (Merck) and triethanolamine, TEA, (Merck) were used to scavenge electrons and holes, respectively, at 1 mM concentration.

2.3.6. Reusability experiments for dichromate reduction

The ability of the system to photoreduce Cr(VI) was tested over five consecutive cycles. In particular, at the end of each experiment, the ZnO@Au nanostructures were recovered by centrifugation, rinsed with ultrapure water, dried at room temperature, and reused. The Cr(VI) reduction efficiency was evaluated according to the procedure previously described.

3. Results and Discussion

3.1. Ultrasound-Assisted Formation of ZnO@Au Hybrid Nanostructures

As previously reported in the literature [26], the ZnO semiconductor employed in this synthetic protocol exhibits piezoelectric characteristics, which play a crucial role in the rapid reduction of Au ions and the formation of the ZnO@Au hybrid. More specifically, the use of ultrasound stimulation in the proposed protocol serves a dual purpose: it facilitates the diffusion of Au ions within the semiconductor matrix and, on the other hand, the formation and implosion of cavitation bubbles in the ultrasonic bath promote the generation of a piezopotential in the piezoelectric material, thereby influencing and enhancing the reduction of Au^{3+}, as will be detailed below.

Before delving into the characterization of the hybrid materials obtained under ultrasound stimulation, a colloidal suspension of ZnO in the presence of an Au precursor solution was subjected to various external stimuli and analyzed via Raman and TEM. Specifically, ZnO nanostructures were investigated after immersion for 10 min in an Au^{3+} precursor solution under different conditions: in the dark without external stimulation and under white light illumination without mechanical stimulation. As shown in Figures S1a-c, none of these conditions resulted in significant morphological, spectroscopic, or structural variations.

However, distinct changes were observed when ZnO/$HAuCl_4$ mixtures at four different weight ratios (named A1, B1, C1 and D1, see Experimental Section) in water were subjected to just one minute of ultrasound stimulation at 42 kHz. Figure 1a-d suggests that the ZnO nanostructures, which initially appear completely white in image (a), change color as a function of the dissolved Au precursor concentration. A progressive decrease of the UV–Vis baseline was observed upon Au functionalization, which can be ascribed to suppression of light scattering by ZnO nanostructures rather than the appearance of new absorption bands (Figure S2).

The morphology of the ZnO structures, in agreement with previous reports [26], consists of thin sheets approximately 50 nm thick, with lateral dimensions of about 0.6 μm (Figure 1e, S3). These highly anisotropic structures are particularly susceptible to deformation upon the implosion of a cavitation bubble, thereby facilitating the generation of a significant piezopotential [26,29]. TEM analysis (Figures 1e–h) suggests the presence of spheroidal nanostructures decorating the ZnO surfaces across all Au precursor concentrations. The images clearly reveal differences in nanoparticle size distribution and surface coverage as a function of precursor concentration. In the lowest-loading sample (B1), AuNPs appear as discrete, well-separated particles with a mean diameter of ~6 ± 3 nm, uniformly decorating the nanoflower petals (Figure 1f). Increasing the Au content (C1) results in larger nanoparticles (~10 ± 5 nm) and a higher surface density, with a tendency toward partial coalescence (Figure 1g). In the highest-loading sample (D1), the AuNPs reach ~18 ± 3 nm, and occasional aggregates form continuous patches along the ZnO edges (Figure 1h). In Figure S4, the size distribution of the Au nanostructures for samples B1, C1, and D1 is shown. The bright–dark contrast between AuNPs and the underlying ZnO substrate, as well as the sharply defined particle contours, supports their metallic nature and distinct phase separation.

The nature of these nanostructures decorating the ZnO surface was

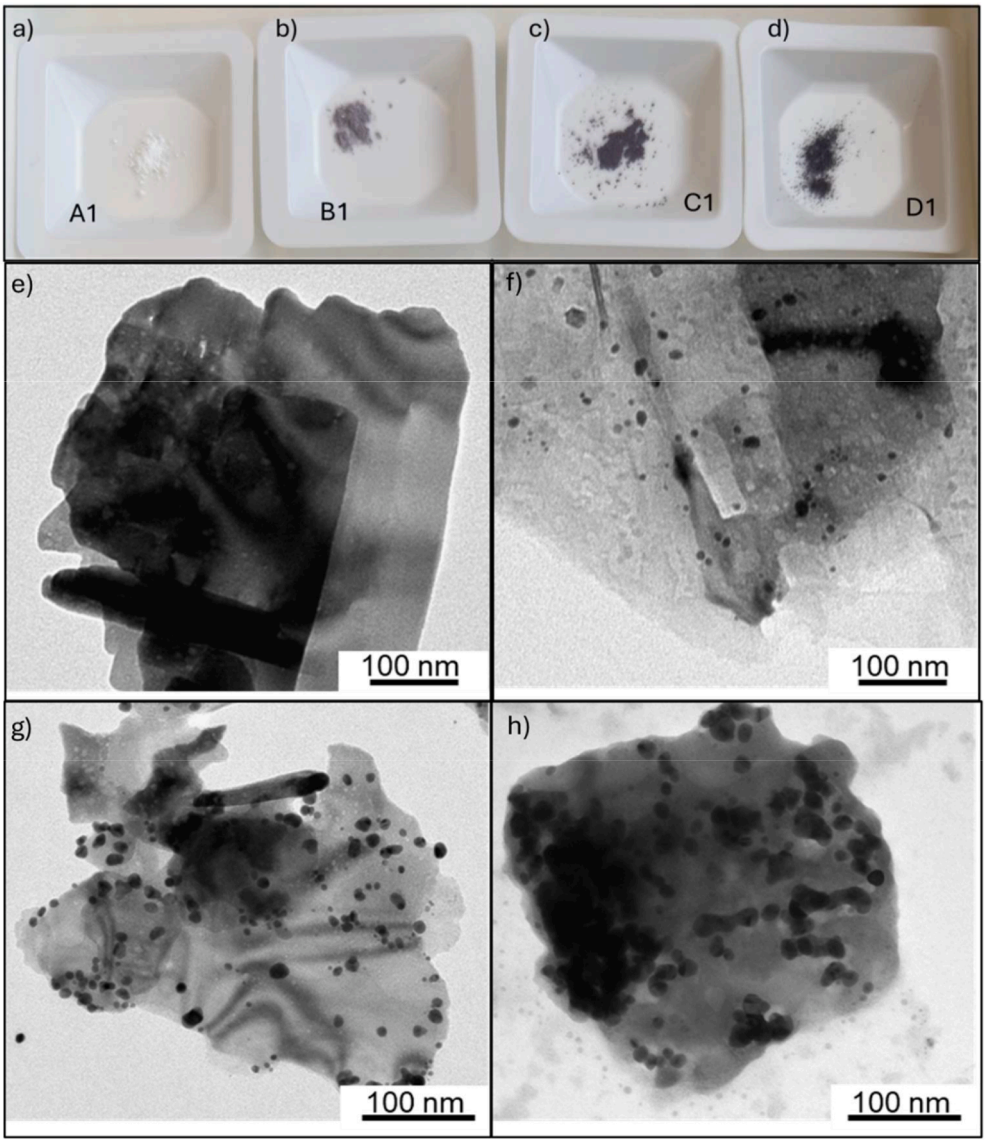

Figure 1. (a-d) Digital photographs of A1, B1, C1 and D1 samples, underlining the color variation depending on Au precursor concentration; TEM images of sample A1 (e), B1 (f), C1 (g) and D1 (h).

investigated using X-ray diffraction (Figure 2a). The diffraction profile of sample B1 closely matches that of pristine ZnO, with peaks at 31.75°, 34.39°, and 36.21°, corresponding to the (100), (002), and (101) planes of wurtzite ZnO, respectively (JPCDS 36-1451). Interestingly, at higher Au precursor concentrations, a peak at 38.1° appears, characteristic of the (111) plane of gold nanostructures [30], confirming the formation of AuNPs. A noteworthy rationalization of this phenomenon emerges from the observation that all three characteristic ZnO peaks shift towards higher angles (in Figure 2b X-ray diffractogram was reported just for the (101) peak in order to easily quantify the peak shift), suggesting lattice strain due to the incorporation of gold ions beneath the semiconductor surface. In particular, the Au ion has a smaller ionic radius (about 0.85 Å) compared to Zn (about 0.88 Å) [31], implying that Zn substitution by Au may induce lattice contraction. This results in a reduction of interplanar distances, justifying the observed XRD peak shift. Moreover, if a small fraction of AuNPs forms within the lattice, they could generate internal stress, further contributing to the peak shift in ZnO [32].

Raman spectroscopy, a powerful technique for probing the crystalline lattice through atomic vibration modes, was performed on all four samples within the 150–750 cm^{-1} range (Figure 2c). The Raman spectrum of sample A1 shows by the characteristic signals of nanostructured wurtzite ZnO, consistent with XRD observations. Notably, a strong peak at 430 cm^{-1}, attributed to the E_{2h} vibrational mode, dominates the spectrum [26]. The $2E_2$ mode at 327 cm^{-1} and the A_1(TO) mode at 380 cm^{-1} [33] are also observed. Additionally, the A_1(LO) mode appears at 575 cm^{-1}. Upon ultrasound treatment, the intensities of the 430 cm^{-1} and 380 cm^{-1} peaks decrease as a function of gold concentration. Both peaks are associated with vibrational modes of the ZnO wurtzite basal plane. Furthermore, a significant reduction in the E_{2h} signal intensity indicates lattice disorder, likely due to Zn substitution by Au, as inferred from the XRD data. This structural distortion weakens the E_{2h} signal. Another plausible explanation for this attenuation is the introduction of oxygen vacancies, Zn interstitials, or other defects that disrupt lattice symmetry and coherence.

Conversely, the A_1(LO) mode intensifies with increasing free carrier concentration. This phenomenon is typical in doped ZnO with high defect densities [34], where A_1(LO) can become highly pronounced due to plasmonic coupling. The same defects, such as oxygen vacancies or Zn interstitials, can amplify the A_1(LO) signal due to their strong coupling with longitudinal optical modes. Thus, Raman spectra fully corroborate XRD findings, indicating that gold ions and/or AuNP formation influence ZnO at both surface and sub-surface levels.

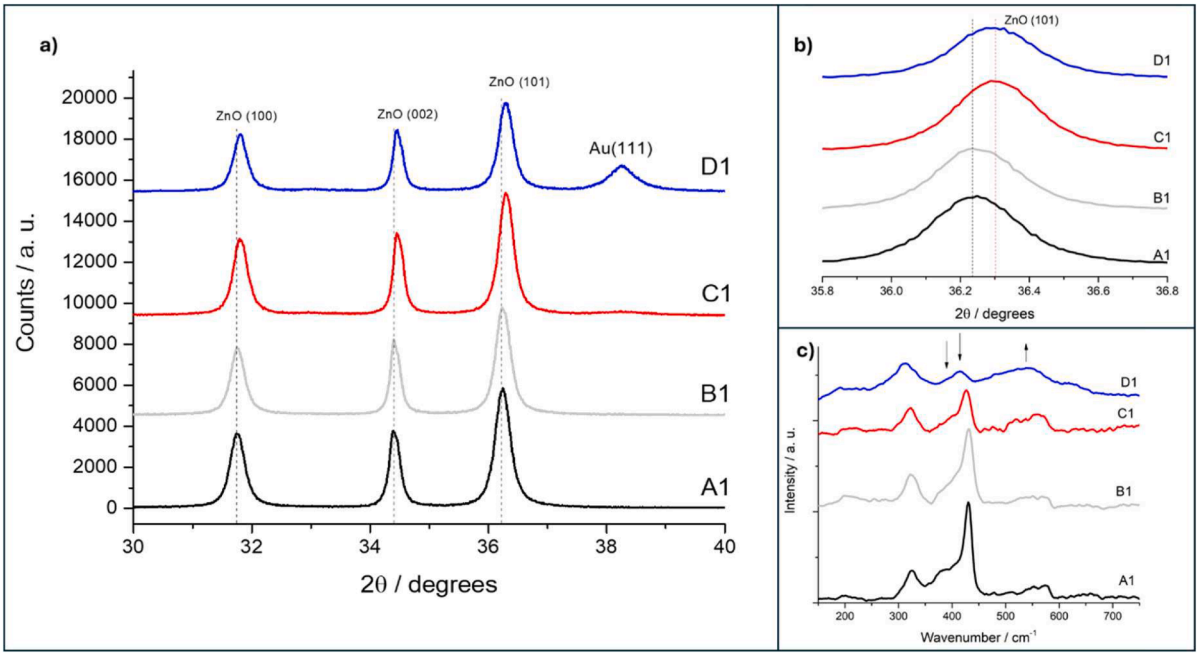

Figure 2. a) X-ray diffractograms obtained for the 4 powdered samples; b) 2θ range magnification of the X-ray diffractograms; c) Raman spectra of the 4 powdered samples in the 100-800 cm^{-1} range.

The observed nanoparticle dimensions and distribution trends align with the crystallographic evidence of Au (111) reflections and the wurtzite ZnO peak shifts. The progressive broadening and shift in XRD peaks, together with Raman mode attenuation, are coherent with the increasing lattice strain and defect density induced by Au incorporation—effects that are also reflected in morphological alterations such as edge roughening and local contrast variations.

This integrated morphological–structural analysis reinforces the conclusion that AuNP nucleation and growth occur directly on the ZnO surfaces via the piezoelectrically-assisted route, producing a well-distributed hybrid interface whose properties can be tuned simply by controlling the precursor concentration.

These findings underscore the remarkable simplicity and controllability of modulating Au nanostructure density and size via such a rapid ultrasound-driven approach. They also highlight how the use of appropriately designed piezoelectric materials can serve a dual role as both a substrate for promoting the synthesis of metal nanoparticles and as a material itself.

3.2. *Mechanism of ZnO@Au Hybrid Nanostructure Formation*

The only external stimulus capable of promoting the formation of ZnO decorated with Au nanostructures is represented by ultrasound (US) [21,35]. The use of US to facilitate the diffusion of metal ions within porous matrices is widely reported in the literature, although this stimulus is always followed by a subsequent step of light irradiation or alternative stimulation [36] to promote the reduction of ionic species. In the present case, however, the application of US for just 1 min appears necessary and sufficient for the formation of the metallic NPs.

As demonstrated in previous studies [29,37], the implosion of cavitation bubbles generated by ultrasound in an aqueous environment leads to an energy release sufficient to induce a structural deformation of ZnO, as used in this synthesis. Consequently, a piezopotential is generated across the ZnO due to a temporary accumulation of charges at the material's edges. This phenomenon not only influences the movement of free charge carriers within ZnO but also induces an accumulation of charged species on its outer surface. Based on this evidence, it is reasonable to hypothesize that the generation of the piezopotential is the key phenomenon driving the reduction of Au^{3+} ions. It has been reported in the literature the synthesis of Au nanoparticles assisted by ultrasound, even though in any cases the presence of organic precursors that assists to the synthesis is crucial [38]. In the present case, more specifically, two different mechanisms can be proposed, which are not necessarily mutually exclusive but rather likely act together in the formation of gold nanostructures:

i) The mechanical stress induced by the implosion of cavitation bubbles leads to the formation of piezo-charges at the semiconductor interface. These charges influence the movement of free carriers within ZnO, which, being an n-type semiconductor, can participate in the reduction of Au^{3+} ions (Figure 3a).
ii) The formation of screening charges [39] at the interface provides a local source of electrons in proximity to the Au^{3+} ions, facilitating their reduction (Figure 3b).

To further confirm the crucial role of piezopotential in the formation of the AuNPs, a control experiment was conducted using TiO_2 (the commercial titania named P25), a material lacking piezoelectric properties. The bare TiO_2 and TiO_2 mixed with Au^{3+} were sonicated in the dark for one minute under identical conditions as samples A1, B1, C1, and D1. TEM analyses (Figures S5a and b) showed no evidence of AuNPs deposition on TiO_2, consistent with previous literature. In fact, it is well established that for materials such as TiO_2, energy input via light or heat following sonication is required to induce the reduction of Au^{3+} ions adsorbed on the semiconductor surface [40].

The role of mechanical stimulation was investigated in another control experiment by subjecting ZnO nanostructures to vigorous stirring (1000 rpm for 1 min) without ultrasound in the presence of Au^{3+} at the highest concentration, corresponding to sample D1. Under these conditions, the nanostructures are undoubtedly exposed to mechanical stress, although it is significantly weaker than that generated by the implosion of cavitation bubbles. It is interesting to note that Raman spectroscopy, similar to what was observed for the B1, C1 and D1 samples, reveals significant changes in the Raman spectrum (Figure 3c), although the variations are less pronounced than those observed in samples treated with US. This result suggests that even such weak

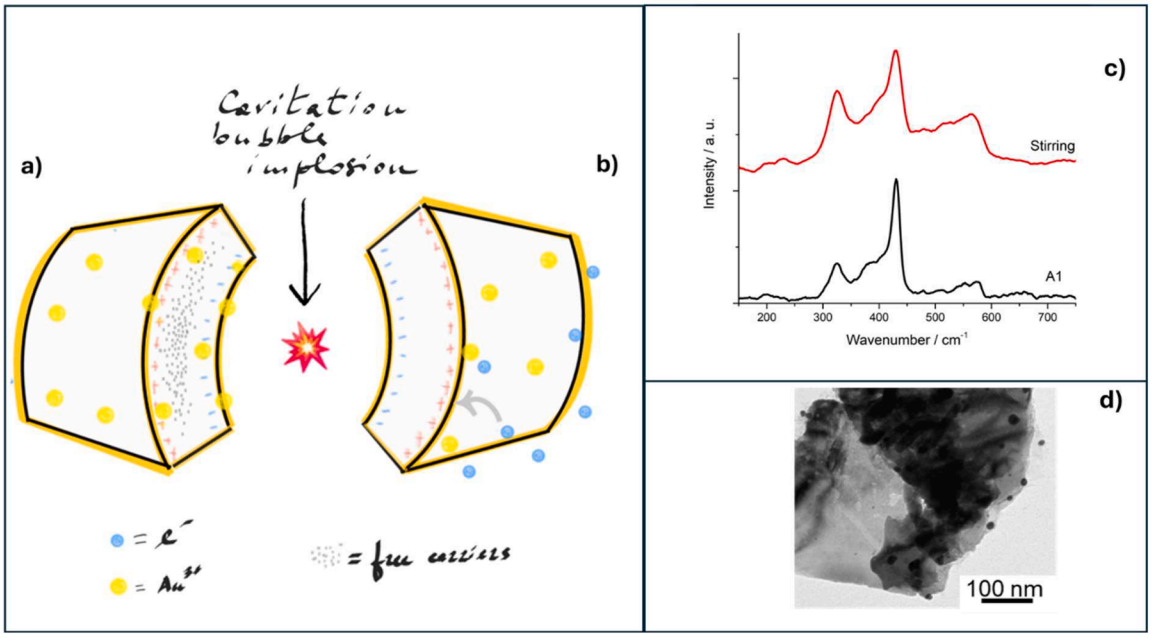

Figure 3. Schematization of Au^{3+} reduction over ZnO structures promoted by the mechanical stress induced by the implosion of cavitation bubbles leads to the formation of piezo-charges at the semiconductor interface (a) and/or the formation of screening charges at the interface (b); c) comparison of Raman spectra of A1 and the sample stirred for 1 min; d) TEM image of the stirred sample.

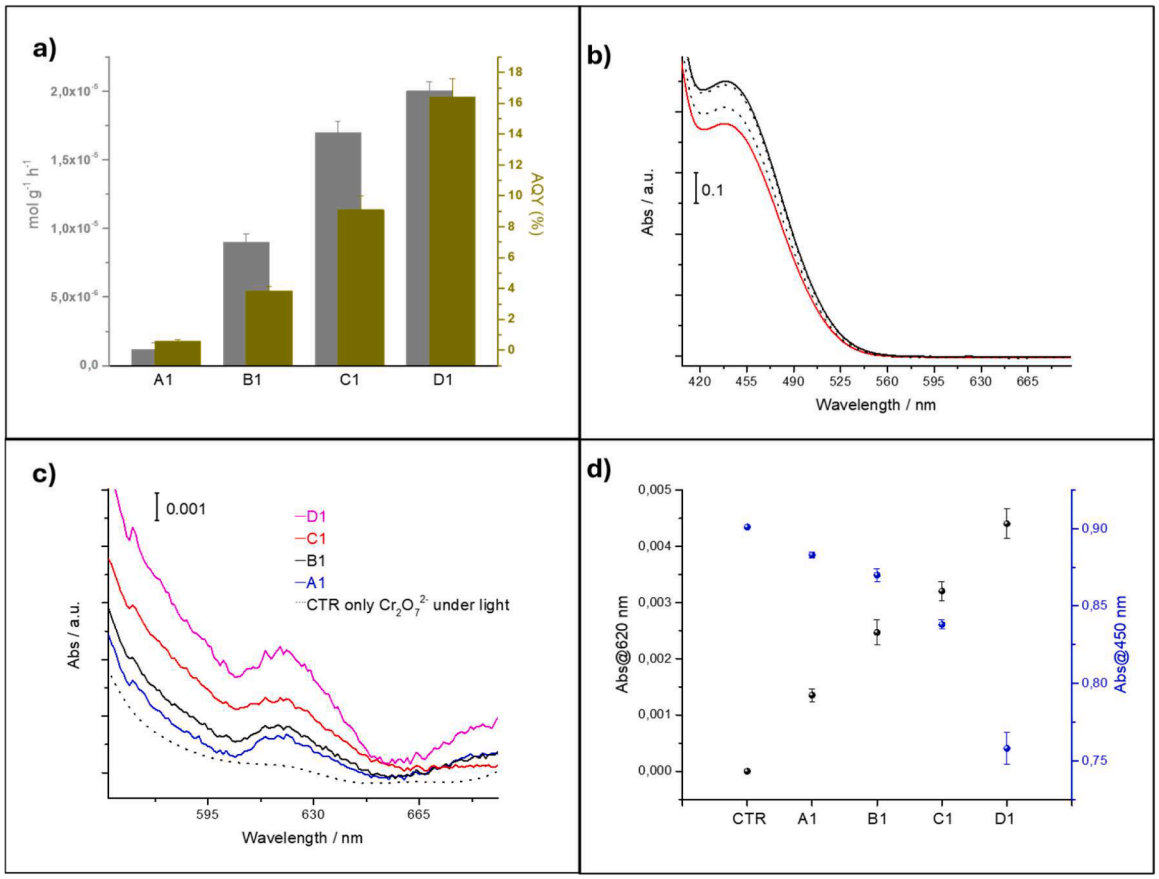

Figure 4. a) H_2O_2 production rate (mol g^{-1} h^{-1}, grey bars) and AQY% (green bars) for the investigated samples; b) bleaching of the signal located at 450 nm monitored every 10 min during 30 min illumination for D1 catalyst; c) increasing of the signal at 620 nm after 30 min illumination for all the samples; d) comparison of the bleaching of the signal at 450 nm and the increasing of the absorbance at 620 nm after 30 min for all the investigated samples.

mechanical stress can induce the formation of nanostructures. Further supporting this observation, TEM images show rare formations, likely attributable to gold nanostructures, decorating the ZnO nanostructures (Figure 3d).

3.3. Photocatalytic Applications

3.3.1. H_2O_2 Production

AuNPs deposited on photo-catalysts, AuNPs have shown to improve oxygen reduction reaction (ORR) efficiency by accelerating electron transfer rates and reducing charge recombination [41,42]. For these reasons, the synthetized systems A1, B1, C1, and D1, were tested for the photocatalytic production of H_2O_2, which was monitored by means of the POD-KI assay, determining the concentration of produced H_2O_2 by measuring its reaction with potassium iodide (KI) in the presence of horseradish peroxidase (POD) as reported in the Experimental Section. The formation of triiodide was spectrophotometrically monitored: the intensity of the peak localized at 350 nm increases in function of the H_2O_2 standard solution concentration allowing obtaining a calibration curve (Figure S6a). Figure S6b reports the spectral profile of the formation of triiodide because of photocatalytic H_2O_2 production upon white light illumination of the sample A1 (black line), B1 (blue line), C1 (red line) and D1 (green line). The H_2O_2 production rates were then expressed in $mol \cdot g^{-1} \cdot h^{-1}$, providing a measure of the photocatalytic activity of the tested systems and the obtained results are reported in Figure 4a (grey bars). H_2O_2 production efficiency was demonstrated to increase with AuNPs size and coating density, following the order A1 < B1 < C1 < D1, according to the spectra reported in Figure S6b.

The presence of larger AuNPs could enhance the Schottky barrier effect, minimizing electron-hole recombination and promoting longer charge carrier lifetimes [41,43]. The enhanced catalytic activity of D1 could be attributed to the larger AuNPs (≥15 nm), which facilitated efficient charge transfer at the ZnO-Au interface.

The higher production rate obtained for D1, $2 \cdot 10^{-5}$ mol g^{-1} h^{-1}, demonstrated the great potential of the developed system, being comparable to the recent literature for photocatalytic hydrogen peroxide production over ZnO-based materials [42,44–48]. It is important to emphasize that the achieved performance is in line with similar systems reported in the literature (Table S1), although the synthesis of the ZnO@Au hybrid presented here is obtained through an extremely low-impact, eco-friendly approach, requiring just one minute of sonication. Additionally, all measurements were performed in pure Milli-Q water, without the use of sacrificial agents or O_2 bubbling to enhance the process, unlike most ZnO–Au systems previously reported. These advantages highlight the valuable compromise achieved with our method, which, while maintaining a comparable production rate, significantly reduces the environmental impact and synthesis time, paving the way for more sustainable and scalable photocatalytic applications.

From this, the apparent quantum yield (AQY%) was calculated for each sample under light irradiation (Figure 4a, green bars) as detailed in the Experimental section. The AQY% also showed a trend of higher efficiency for samples with larger AuNPs: D1 exhibited the highest AQY%, followed by C1, B1, and A1. In contrast, smaller AuNPs (B1) demonstrated lower AQY%, which might be related to their smaller size, lower electron extraction efficiency, and less efficient charge separation compared to their larger counterparts. Achieving good AQY% values is crucial as it directly reflects the efficiency of a photocatalyst in converting incident light into the desired chemical reaction. A higher AQY% indicates a more effective utilization of photons, leading to enhanced reaction rates and improved energy conversion efficiency [28]. The balance between efficiency and sustainability can be further emphasized by the notable AQY% obtained, reaching up to 16% for D1. Despite the rapid and low-impact synthesis approach, the system maintains a competitive AQY%, reinforcing its potential for practical applications where both performance and environmental considerations are crucial.

To assess the possible contribution of plasmonic enhancement, A1 and D1 samples were tested under UV-filtered illumination with a cut-off at 415 nm (Figure S7). Under these conditions, only a very weak H_2O_2 signal was detected, about 20 times lower than that obtained in the presence of the catalyst under full illumination. This negligible response suggests that the photocatalytic activity of the ZnO@Au hybrids is dominated by UV-driven processes, with no significant contribution from localized surface plasmon resonance (LSPR) effects of AuNPs. This finding aligns with previous reports that emphasized the importance of semiconductor–metal charge transfer over plasmonic field enhancement in ZnO-based photocatalysis [49]. The role of the AuNPs therefore appears to be mainly devoted to their function as electron sinks and catalytic sites rather than as plasmonic enhancers. Nevertheless, we cannot completely rule out a minor plasmonic contribution under visible excitation, but its magnitude is negligible compared to the dominant UV-driven pathway.

Finally, to evaluate the stability and reusability of the D1 catalyst, we conducted a recycling experiment, performing four consecutive photocatalytic cycles (Figure S8). Remarkably, D1 maintained its high efficiency in H_2O_2 production across the first 3 cycles, demonstrating its strong stability under continuous illumination with a slight decrease in activity over the fourth cycle. This behavior emphasizes the robustness of the D1 catalyst for practical, long-term applications in photocatalytic H_2O_2 production.

3.3.2. Dichromate Photoreduction over ZnO@Au hybrids

To further validate the catalytic versatility of the ultrasound-synthesized ZnO@Au nanostructures beyond hydrogen peroxide photoproduction, we investigated their ability to reduce hexavalent chromium (Cr(VI)), a well-known model pollutant. The Cr(VI) photoreduction test also serves as a benchmark to probe the efficiency of interfacial charge separation and electron transfer, which are critical for environmental photocatalysis [50].

Aqueous suspensions containing $K_2Cr_2O_7$ (3 mM, pH adjusted to ~4 with H_2SO_4 0.1 M) and 0.6 g L^{-1} of the catalysts (A1–D1) were irradiated under simulated solar light. The reduction of Cr(VI) to Cr(III) was monitored spectrophotometrically by the bleaching of the absorption band at 450 nm, characteristic of Cr(VI) species and the increasing of the signal located at 620 nm characteristic of Cr(III) (Figure 4b and 4c for D1 sample and Figure S9 for the other catalysts). No significant reduction occurred in the dark or in the absence of catalyst (named CTR), confirming the photodriven nature of the process.

As shown in Figure 4d, the photoreduction efficiency followed the same trend observed for H_2O_2 generation, with D1 exhibiting the most pronounced decrease in absorbance at 450 nm and increase in absorbance at 620 nm, followed by C1, B1, and A1.

After 30 minutes of illumination, sample D1 achieved over 20% conversion of Cr(VI), while the less Au-decorated sample B1 showed only ~5% reduction. This result correlates well with the enhanced charge separation observed in fluorescence quenching experiments, that will be discussed in the next paragraph.

The improved performance of D1 can be attributed to the higher density and size of AuNPs, which enhance interfacial electron transfer via more efficient Schottky junctions. These findings confirm that the ZnO@Au interface, engineered via an ultra-rapid piezoelectric route, is not limited to one specific reaction but can be applied across redox pathways, including Cr(VI) reduction and oxygen-to-H_2O_2 conversion.

To evaluate the stability and reusability of the D1 catalyst, a recycling test was carried out through four consecutive photoreduction cycles (Figure S10). The catalyst retained a high Cr(VI) reduction efficiency during the first three cycles, whereas a marked decrease in activity was recorded in the fourth and fifth runs. This decline can be ascribed to the low pH conditions required to maintain Cr in its hexavalent state. Indeed, in acidic environments the crystalline structure of ZnO can undergo degradation, potentially inducing significant alterations in both the chemical composition and the physical properties of

the ZnO@Au hybrid material.

This additional proof-of-concept consolidates the proposed interface as a robust and generalizable photocatalytic platform.

3.3.3. Photocatalytic Mechanism

The Oxygen Reduction Reaction (ORR) can produce hydrogen peroxide (H_2O_2) through a 2-electron process, where oxygen is reduced directly to H_2O_2 in two steps. In contrast, the Water Oxidation Reaction (WOR), which typically produces oxygen, can lead to H_2O_2 formation under specific catalytic conditions. During WOR, intermediate species such as hydroxyl radicals (•OH) and other reactive oxygen species can form and subsequently combine to produce H_2O_2 [28]. So, to understand which catalytic mechanism was envisaged for hydrogen peroxide evolution, ascorbic acid (AA) was chosen as superoxide anion scavenger and isopropanol (IPA) was used as hydroxyl radicals' scavenger [51]. The introduction of AA completely inhibited H_2O_2 production (Figure S11a) for all the samples, suggesting that the photocatalytic reaction follows a sequential two-step one-electron ORR pathway:

First electron transfer: $O_2 + e^- \rightarrow O_2^{\bullet-}$ (superoxide anion)

Second electron transfer: $O_2^{\bullet-} + e^- + 2H^+ \rightarrow H_2O_2$

In contrast, IPA led to increased H_2O_2 production (Figure S11b), with the effect being most pronounced in B1, followed by A1, and least affected in D1. To better underline this, the molar concentration of produced H_2O_2 in the experiment carried out in presence of AA (black bars) and IPA (red bars) were plotted into the histogram reported in Figure 5a. It is worth highlighting that B1 in presence of IPA reached a production rate almost comparable to the most performing catalysts, C1 and D1. This suggested that hydroxyl radicals act as competing species in the reaction pathway [52]. Their suppression so enhances the selectivity for H_2O_2 generation, particularly in B1 characterized by smaller AuNPs (~3–6 nm), which showed fewer recombination losses and a more efficient electron flow in presence of the scavenger.

Steady-state fluorescence measurements at 370 nm excitation are reported in Figure 5b and showed fluorescence quenching, with the most pronounced quenching observed for D1 and C1, followed by B1, if compared to A1, pristine ZnO. This behaviour can be considered a direct indication of enhanced charge transfer efficiency from ZnO to noble metal nanoparticles [49]. These findings aligned with the results obtained monitoring the hydrogen peroxide production with a UV filter, since no plasmonic effect is taking place. This evidence supports the proposed mechanism (Figure 5c), where ZnO acts as an electron donor to Au nanoparticles. Au, serving also as a cocatalyst, promotes the one-electron, two-step ORR, ultimately leading to efficient H_2O_2 generation. As discussed, Raman analyses revealed a decrease in ZnO vibrational modes located at 430 cm^{-1} and 380 cm^{-1} as AuNPs concentration increases, indicative of lattice disorder and defect generation, and XRD peak shifts suggested the incorporation of Au ions into the ZnO lattice. Defects can act as charge trap sites [53], stabilizing intermediates and promoting a more selective ORR pathway in C1 and D1. This reduces the likelihood of the undesired water oxidation reaction (WOR), as reflected in the reduced influence of IPA in these samples, suggesting that fewer hydroxyl radicals are formed, which in turn promotes H_2O_2 formation.

Also the photocatalytic reduction of Cr(VI) was deeply studied to comprehend if a plasmonic effect took place and performing the reaction in presence of scavenging species. First of all, in order to exclude ZnO UV activation and to understand the role of AuNPs in the catalytic process, D1 sample was irradiated with visible light using a 415 nm cut-off filter. The catalyst activity drastically reduced from 20% to 1.5%, confirming that the Au component does not contribute via plasmonic excitation under these conditions, and that ZnO remains the active UV-responsive

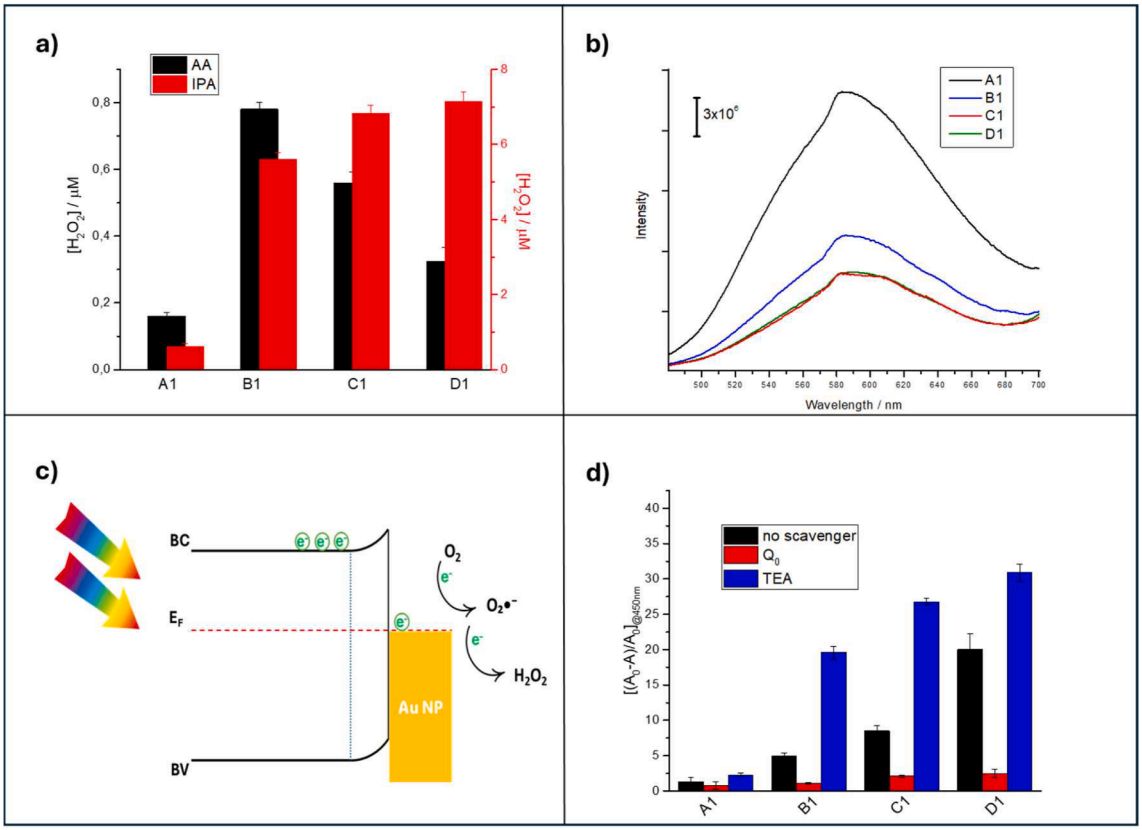

Figure 5. a) Molar concentration of produced H_2O_2 over the four samples in presence of AA (black bars) and IPA (red bars); b) steady state fluorescence spectra upon 370 nm excitation of 0.6 g L^{-1} samples water suspension; c) Schematic representation of the band diagram of ZnO@Au and mechanism of H_2O_2 photoproduction; d) bleaching of the band localized at 450 nm plotted as $\frac{A_0-A}{A_0} \times 100$, where A is the absorbance recorded after 30 min and A_0 is the absorbance at the starting point.

phase. This observation is consistent with fluorescence quenching data, which indicate that Au nanoparticles act as electron sinks, facilitating charge separation rather than direct photoactivation.

Considering that the photoreduction process takes place according to the reaction:

$$Cr_2O_7^{2-} + 14\ H^+ + 6e^- \rightarrow 2Cr^{3+} + 7H_2O$$

p-benzoquinone (Q_0) and triethanolamine (TEA) were chosen as electron and holes scavengers [49,54], respectively, to elucidate the mechanism.

The introduction of Q_0 significantly inhibited the reaction, with reduction yields dropping to 0.8% for A1 and only 2.5% for D1 (Figure 5d, black bars no scavenger and red bars Q_0) supporting the key role of photogenerated electrons in Cr(VI) reduction. In contrast, the addition of TEA substantially enhanced the reaction across all samples, yielding up to 30.9% reduction with D1 (Figure 5d, blue bars TEA). The observed enhancement (e.g., from 20.0% to 30.9% in D1) suggests that effective removal of photoinduced holes minimizes charge recombination and increases electron availability. Interestingly, despite D1 showing the highest Cr(VI) reduction performance, it exhibits reduced activity in water oxidation, suggesting that lower hole consumption by side reactions (e.g., O_2 evolution) may contribute to better charge utilization for Cr(VI) reduction. These results highlight the synergistic effect of Au incorporation and selective hole scavenging in optimizing ZnO-based photocatalysts for photoreductive applications.

In conclusion, the photocatalytic behavior observed clearly highlights the central role of the ZnO–Au interface in driving the overall mechanism. The Au nanoparticles efficiently extract photogenerated electrons from ZnO, enhancing charge separation without relying on plasmonic activation. This interfacial architecture minimizes recombination losses and improves electron availability for surface reactions. The developed heterojunction thus proves essential in enabling and directing the photocatalytic response under UV excitation.

4. Conclusions

In this work, we demonstrated a fast, green, and scalable method for engineering ZnO@Au hybrid interfaces through ultrasound-driven, piezoelectrically-assisted synthesis. This one-minute, reagent-free protocol harnesses the intrinsic piezoelectricity of ZnO to induce the in situ reduction of gold ions, forming well-integrated Au nanoparticles without the need for external stimuli such as heat, light, or chemical reductants. Structural and spectroscopic analyses confirm the interfacial coupling between the metal and semiconductor, with modifications extending from the surface to the sub-surface region.

The resulting ZnO@Au hybrids exhibit strong photocatalytic performance in two benchmark redox reactions, hydrogen peroxide production and Cr(VI) photoreduction, highlighting the versatility and functional relevance of the designed interface. Notably, the catalytic activity and selectivity can be tuned by modulating nanoparticle size and distribution through simple variation in precursor concentration. Mechanistic insights, supported by scavenger tests and fluorescence quenching, confirm that the photocatalytic enhancement arises from efficient charge separation and electron transfer at the ZnO–Au junction, rather than plasmonic effects.

Overall, this study introduces a paradigm shift in the fabrication of hybrid photocatalysts, offering an ultra-rapid, low-impact, and highly effective route to interface design. The generalizability of the approach opens new opportunities for applications in environmental remediation, sustainable chemical production, and advanced materials engineering.

CRediT authorship contribution statement

Simona Bettini: Writing – review & editing, Supervision, Methodology, Conceptualization. **Gabriele Manca:** Writing – original draft, Methodology, Investigation. **Rosanna Pagano:** Writing – original draft, Methodology, Conceptualization. **Chiara Ingrosso:** Methodology, Investigation. **Donato Valli:** Methodology, Investigation, Conceptualization. **Johan Hofkens:** Writing – review & editing, Conceptualization. **Maarten Roeffaers:** Writing – review & editing, Conceptualization. **Ludovico Valli:** Supervision, Funding acquisition, Conceptualization. **Gabriele Giancane:** Writing – review & editing, Supervision, Methodology, Conceptualization.

Declaration of competing interest

The authors declare that they have no known competing financial interests or personal relationships that could have appeared to influence the work reported in this paper.

ACKNOWLEDGMENT

This research was supported by the PRIN 2022 (protocol number 20228YFRNL), by the PRIN PNRR 2022 (protocol number P2022WLAY7) and by the Spoke 9 – Cascade Call under the project NANOCARB: High-surface-area carbon nanostructures as electronic transducers for artificial photosynthesis, funded by PNRR, MISSION 4 - Network 4 Energy Sustainable Transition (CUP B53C22004060006). D. V. acknowledges financial support from the Research Foundation Flanders as FWO doctoral fellowship (FWO Grant Number 1S45223N).

Supplementary materials

Supplementary material associated with this article can be found, in the online version, at doi:10.1016/j.surfin.2025.107611.

Data availability

Data will be made available on request.

REFERENCES

[1] L. Amirav, M. Wächtler, Nano Schottky?, Nano Lett 22 (2022) 9783–9785, https://doi.org/10.1021/acs.nanolett.2c04150.
[2] Y. Ben-Shahar, D. Stone, U. Banin, Rich Landscape of Colloidal Semiconductor–Metal Hybrid Nanostructures: Synthesis, Synergetic Characteristics, and Emerging Applications, Chem. Rev. 123 (2023) 3790–3851, https://doi.org/10.1021/acs.chemrev.2c00770.
[3] A.D. Terna, E.E. Elemike, J.I. Mbonu, O.E. Osafile, R.O. Ezeani, The future of semiconductors nanoparticles: Synthesis, properties and applications, Materials Science and Engineering: B 272 (2021) 115363, https://doi.org/10.1016/j.mseb.2021.115363.
[4] S.-C. Hung, Y.-H. Lee, Enhanced glucose sensing via nanoparticles-modified extended gates: A novel approach to electric double layer modulation and signal amplification in field effect transistors for improved detection sensitivity, Biosensors and Bioelectronics: X 23 (2025) 100576, https://doi.org/10.1016/j.biosx.2025.100576.
[5] L. Yuan, Z. Geng, J. Xu, F. Guo, C. Han, Metal-Semiconductor Heterostructures for Photoredox Catalysis: Where Are We Now and Where Do We Go? Advanced Functional Materials 31 (2021) 2101103 https://doi.org/10.1002/adfm.202101103.
[6] A. Gellé, T. Jin, L. de la Garza, G.D. Price, L.V. Besteiro, A. Moores, Applications of Plasmon-Enhanced Nanocatalysis to Organic Transformations, Chem. Rev. 120 (2020) 986–1041, https://doi.org/10.1021/acs.chemrev.9b00187.
[7] L. Zhang, D. Zhu, H. He, Q. Wang, L. Xing, X. Xue, Enhanced piezo/solar-photocatalytic activity of Ag/ZnO nanotetrapods arising from the coupling of surface plasmon resonance and piezophototronic effect, Journal of Physics and Chemistry of Solids 102 (2017) 27–33, https://doi.org/10.1016/j.jpcs.2016.11.009.
[8] R. He, D. Xu, M. Sayed, S-scheme heterojunction-induced surface plasmon response, Journal of Materiomics 11 (2025) 100989, https://doi.org/10.1016/j.jmat.2024.100989.
[9] X. Guo, Y. Fu, D. Hong, B. Yu, H. He, Q. Wang, L. Xing, X. Xue, High-efficiency sono-solar-induced degradation of organic dye by the piezophototronic/photocatalytic coupling effect of FeS/ZnO nanoarrays, Nanotechnology 27 (2016) 375704, https://doi.org/10.1088/0957-4484/27/37/375704.
[10] D. Barman, J. Borah, I. Changmai, P. Pathak, B.K. Sarma, Vibrational Property-Driven NIR Transparency in X:ZnO (X = Mo, Al) Multilayer Transparent Electrodes for Self-Powered Flexible Optoelectronics, ACS Appl. Electron. Mater. 6 (2024) 1666–1681, https://doi.org/10.1021/acsaelm.3c01585.

[11] F. Ge, L. Zheng, Y. Wang, C. Feng, Y. Chen, L. Hu, H. Liu, Y. Yang, L. Ma, F. Cheng, X.-J. Wu, Reversible Photochromic Phenomenon of Plasmonic Metal/Semiconductor Heterostructures via Photoinduced Electron Storage, Nano Lett 24 (2024) 12285–12291, https://doi.org/10.1021/acs.nanolett.4c03564.

[12] Y. Liu, G. Su, W. Wang, H. Wei, L. Dang, A novel multifunctional SERS microfluidic sensor based on ZnO/Ag nanoflower arrays for label-free ultrasensitive detection of bacteria, Anal. Methods 16 (2024) 2085–2092, https://doi.org/10.1039/D4AY00018H.

[13] L. Wang, Y. Gou, M. Liu, X. Yang, L. Fan, M. Wei, H. Liu, J. Yang, F. Wang, L. Yang, Silver nanoparticle/amorphous tantalum nitride antenna for boosting efficiency of perovskite solar cells: Synergistically achieving near-field enhancement and chemical passivation, Solar Energy Materials and Solar Cells 282 (2025) 113417, https://doi.org/10.1016/j.solmat.2025.113417.

[14] L. Rebecchi, I. Martin, I.M. Albo, P. Ranjan, T. Gatti, F. Scotognella, A. Rubino, I. Kriegel, Scalable Production of Metal Oxide Nanoparticles for Optoelectronics Applications, Chemistry A European J 31 (2025) e202401711, https://doi.org/10.1002/chem.202401711.

[15] H. Xu, Z. Wei, F. Verpoort, J. Hu, S. Zhuiykov, Nanoscale Au-ZnO Heterostructure Developed by Atomic Layer Deposition Towards Amperometric H2O2 Detection, Nanoscale Res Lett 15 (2020) 41, https://doi.org/10.1186/s11671-020-3273-7.

[16] M.R. Alfaro Cruz, O. Ceballos-Sanchez, E. Luévano-Hipólito, L.M. Torres-Martínez, ZnO thin films deposited by RF magnetron sputtering: Effects of the annealing and atmosphere conditions on the photocatalytic hydrogen production, International Journal of Hydrogen Energy 43 (2018) 10301–10310, https://doi.org/10.1016/j.ijhydene.2018.04.054.

[17] F. Rasouli, A. Rouhollahi, F. Ghahramanifard, Fabrication of silver nanoparticles decorated zinc oxide nanotubes by electrodeposition technique for photoelectrochemical water splitting, Materials Science in Semiconductor Processing 93 (2019) 371–378, https://doi.org/10.1016/j.mssp.2018.08.004.

[18] C. Li, X. Wang, J. Wu, J. Gao, R. Zhao, S. Xia, H. Yang, Z. Chen, L. Li, W. Wang, Harnessing ultrasound in photocatalysis: Synthesis and piezo-enhanced effect: A review, Ultrasonics Sonochemistry 99 (2023) 106584, https://doi.org/10.1016/j.ultsonch.2023.106584.

[19] M. Carofiglio, N.M. Percivalle, S. Hernandez, M. Laurenti, G. Canavese, J.C. Matos, M.C. Gonçalves, V. Cauda, Ultrasound-assisted water oxidation: unveiling the role of piezoelectric metal-oxide sonocatalysts for cancer treatment, Biomed Microdevices 26 (2024) 37, https://doi.org/10.1007/s10544-024-00720-3.

[20] M.A. Ahmed, Z.M. Abou-Gamra, M.A. ALshakhanbeh, H. Medien, Control synthesis of metallic gold nanoparticles homogeneously distributed on hexagonal ZnO nanoparticles for photocatalytic degradation of methylene blue dye, Environmental Nanotechnology, Monitoring & Management 12 (2019) 100217, https://doi.org/10.1016/j.enmm.2019.100217.

[21] B. Zhong, S. Li, J. Hu, X. Yang, Y. Cai, C.M. Li, J. Qu, Advances in ultrasound-assisted photocatalyst synthesis and piezo-photocatalysts, J. Mater. Chem. A 11 (2023) 22608–22630, https://doi.org/10.1039/D3TA05125K.

[22] X. Xue, W. Zang, P. Deng, Q. Wang, L. Xing, Y. Zhang, Z.L. Wang, Piezo-potential enhanced photocatalytic degradation of organic dye using ZnO nanowires, Nano Energy 13 (2015) 414–422, https://doi.org/10.1016/j.nanoen.2015.02.029.

[23] A. Yu, S. Liu, Y. Yang, Recent advances in electrosynthesis of H_2 O_2 *via* two-electron oxygen reduction reaction, Chem. Commun. 60 (2024) 5232–5244, https://doi.org/10.1039/D4CC01476F.

[24] A. Bhati, S.R. Anand, D. Saini, S.K.Sonkar Gunture, Sunlight-induced photoreduction of Cr(VI) to Cr(III) in wastewater by nitrogen-phosphorus-doped carbon dots, Npj Clean Water 2 (2019) 12, https://doi.org/10.1038/s41545-019-0036-z.

[25] A. Lathe, A.M. Palve, A review: Engineered nanomaterials for photoreduction of Cr (VI) to Cr(III), Journal of Hazardous Materials Advances 12 (2023) 100333, https://doi.org/10.1016/j.hazadv.2023.100333.

[26] S. Bettini, R. Pagano, D. Valli, M. Ottolini, S. Pal, J. Hofkens, M. Roeffaers, G. Giancane, L. Valli, Tailoring of Zinc Oxide-based microstructures to efficiently promote piezocatalytic water oxidation and oxygen production, Journal of Environmental Chemical Engineering 12 (2024) 114312, https://doi.org/10.1016/j.jece.2024.114312.

[27] M. Wang, S. Qiu, H. Yang, Y. Huang, L. Dai, B. Zhang, J. Zou, Spectrophotometric determination of hydrogen peroxide in water with peroxidase-catalyzed oxidation of potassium iodide and its applications to hydroxylamine-involved Fenton and Fenton-like systems, Chemosphere 270 (2021) 129448, https://doi.org/10.1016/j.chemosphere.2020.129448.

[28] X. Fang, X. Huang, Q. Hu, B. Li, C. Hu, B. Ma, Y. Ding, Recent developments in photocatalytic production of hydrogen peroxide, Chem. Commun. 60 (2024) 5354–5368, https://doi.org/10.1039/D4CC01577K.

[29] S. Bettini, R. Pagano, D. Valli, C. Ingrosso, M. Roeffaers, J. Hofkens, G. Giancane, L. Valli, ZnO nanostructures based piezo-photocatalytic degradation enhancement of steroid hormones, Surfaces and Interfaces 36 (2023) 102581, https://doi.org/10.1016/j.surfin.2022.102581.

[30] S. Krishnamurthy, A. Esterle, N.C. Sharma, S.V. Sahi, Yucca-derived synthesis of gold nanomaterial and their catalytic potential, Nanoscale Res Lett 9 (2014) 627, https://doi.org/10.1186/1556-276X-9-627.

[31] W.B. Jensen, The Origin of the Ionic-Radius Ratio Rules, Journal of Chemical Education 87 (2010) 587–588, https://doi.org/10.1021/ed100258f.

[32] Y. Xu, H.Z. Wang, Influence of Au doping concentration on structural and optical properties of ZnO:Au films fabricated through magnetron sputtering, Optical Materials 108 (2020) 110433, https://doi.org/10.1016/j.optmat.2020.110433.

[33] R.F. Zhuo, H.T. Feng, Q. Liang, J.Z. Liu, J.T. Chen, D. Yan, J.J. Feng, H.J. Li, S. Cheng, B.S. Geng, X.Y. Xu, J. Wang, Z.G. Wu, P.X. Yan, G.H. Yue, Morphology-controlled synthesis, growth mechanism, optical and microwave absorption properties of ZnO nanocombs, J. Phys. D: Appl. Phys. 41 (2008) 185405, https://doi.org/10.1088/0022-3727/41/18/185405.

[34] H.F. Liu, S. Tripathy, G.X. Hu, H. Gong, Surface optical phonon and A1(LO) in ZnO submicron crystals probed by Raman scattering: Effects of morphology and dielectric coating, Journal of Applied Physics 105 (2009) 053507, https://doi.org/10.1063/1.3087482.

[35] S. Xu, L. Guo, Q. Sun, Z.L. Wang, Piezotronic Effect Enhanced Plasmonic Photocatalysis by AuNPs/BaTiO3 Heterostructures, Advanced Functional Materials 29 (2019) 1808737, https://doi.org/10.1002/adfm.201808737.

[36] X. Wang, J.C. Yu, C. Ho, A.C. Mak, A robust three-dimensional mesoporous Ag/TiO 2 nanohybrid film, Chemical Communications 0 (2005) 2262–2264, https://doi.org/10.1039/B500605H.

[37] K. Yasui, Influence of ultrasonic frequency on multibubble sonoluminescence, The Journal of the Acoustical Society of America 112 (2002) 1405–1413, https://doi.org/10.1121/1.1502898.

[38] K. Okitsu, M. Ashokkumar, F. Grieser, Sonochemical Synthesis of Gold Nanoparticles: Effects of Ultrasound Frequency, J. Phys. Chem. B 109 (2005) 20673–20675, https://doi.org/10.1021/jp0549374.

[39] K. Wang, C. Han, J. Li, J. Qiu, J. Sunarso, S. Liu, The Mechanism of Piezocatalysis: Energy Band Theory or Screening Charge Effect? Angewandte Chemie International Edition 61 (2022) e202110429 https://doi.org/10.1002/anie.202110429.

[40] J.C. Yu, L. Zhang, J. Yu, Rapid synthesis of mesoporous TiO2 with high photocatalytic activity by ultrasound-induced agglomeration, New J. Chem. 26 (2002) 416–420, https://doi.org/10.1039/B109173E.

[41] R.H. Adnan, A.A. Jalil, Gold photocatalysis in sustainable hydrogen peroxide generation, Materials Today Chemistry 27 (2023) 101322, https://doi.org/10.1016/j.mtchem.2022.101322.

[42] X. Meng, P. Zong, L. Wang, F. Yang, W. Hou, S. Zhang, B. Li, Z. Guo, S. Liu, G. Zuo, Y. Du, T. Wang, V.A.L. Roy, Au-nanoparticle-supported ZnO as highly efficient photocatalyst for H2O2 production, Catalysis Communications 134 (2020) 105860, https://doi.org/10.1016/j.catcom.2019.105860.

[43] G. Žerjav, M. Roškarič, J. Zavašnik, J. Kovač, A. Pintar, Effect of Au loading on Schottky barrier height in TiO2 + Au plasmonic photocatalysts, Applied Surface Science 579 (2022) 152196, https://doi.org/10.1016/j.apsusc.2021.152196.

[44] S. Kawano, M. Fujishima, H. Tada, Size effect of zinc oxide-supported gold nanoparticles on the photocatalytic activity for two-electron oxygen reduction reaction, Catalysis Communications 144 (2020) 106076, https://doi.org/10.1016/j.catcom.2020.106076.

[45] X. Pang, N. Skillen, D.W. Bahnemann, D.W. Rooney, P.K.J. Robertson, Photocatalytic H2O2 Generation Using Au-Ag Bimetallic Alloy Nanoparticles loaded on ZnO, Catalysts 12 (2022) 939, https://doi.org/10.3390/catal12090939.

[46] X. Sun, G. Zhao, S. Li, J. Liu, M. Huang, Enhanced photocatalytic activity of carbon nitride nanosheets *via* alkali metal ion doping, New J. Chem. 48 (2024) 9231–9242, https://doi.org/10.1039/D4NJ01210K.

[47] F. He, Y. Hu, H. Zhong, Z. Wang, S. Peng, Y. Li, Effect of molten-salt modulation on the composition and structure of g-C_3 N_4 -based photocatalysts, Chem. Commun. 59 (2023) 10476–10487, https://doi.org/10.1039/D3CC03052K.

[48] Y. Wen, H. Che, C. Tang, B. Liu, Y. Ao, A Schottky heterojunction with spatially separated active sites for piezo-photocatalytic dual-channel hydrogen peroxide generation, Nano Energy 128 (2024) 109837, https://doi.org/10.1016/j.nanoen.2024.109837.

[49] R. Pagano, A. Quarta, S. Pal, A. Licciulli, L. Valli, S. Bettini, Enhanced Solar-Driven Applications of ZnO@Ag Patchy Nanoparticles, J. Phys. Chem. C 121 (2017) 27199–27206, https://doi.org/10.1021/acs.jpcc.7b09594.

[50] D. Liu, M.W. Zhang, W.J. Xie, L. Sun, Y. Chen, W.W. Lei, Efficient photocatalytic reduction of aqueous Cr(VI) over porous BNNSs/TiO_2 nanocomposites under visible light irradiation, Catal. Sci. Technol. 6 (2016) 8309–8313, https://doi.org/10.1039/C6CY01770C.

[51] R. Pagano, S. Bettini, M. Ottolini, G. Ciccarella, L. Valli, G. Giancane, Piezo- and photo- responsive ZnO nanostructures for efficient tetracycline water remediation, Colloids and Surfaces A: Physicochemical and Engineering Aspects 680 (2024) 132626, https://doi.org/10.1016/j.colsurfa.2023.132626.

[52] C. Tang, M. Cheng, C. Lai, L. Li, Z. Wei, D. Ma, L. Du, G. Wang, L. Yang, L. Tang, Multiple path-dominated activation of peroxymonosulfate by MOF-derived Fe2O3/Mn3O4 for catalytic degradation of tetracycline, Journal of Environmental Chemical Engineering 11 (2023) 110395, https://doi.org/10.1016/j.jece.2023.110395.

[53] M. Ning, K. Zhao, L. Zhao, S. Cao, J. Zhao, Y. Gao, X. Yuan, Passivating defects in ZnO electron transport layer for enhancing performance of red InP-based quantum dot light-emitting diodes, Materials Research Bulletin 170 (2024) 112589, https://doi.org/10.1016/j.materresbull.2023.112589.

[54] M. Michalík, P. Poliak, V. Lukeš, E. Klein, From phenols to quinones: Thermodynamics of radical scavenging activity of para-substituted phenols, Phytochemistry 166 (2019) 112077, https://doi.org/10.1016/j.phytochem.2019.112077.